AIAA 2000-1040
Icing Analysis and Test of a Business Jet Engine Inlet Duct

K. Al-Khalil, R. Hitzigrath, Cox & Company, Inc.
New York, NY 10014
O. Philippi, VisionAire Corporation
Chesterfield, MO 63005
C. Bidwell, NASA Glenn Research Center
Cleveland, OH 44135

38th Aerospace Sciences
Meeting & Exhibit
10-13 January 2000 / Reno, NV

For Permission to copy or republish, contact the American Institute of Aeronautics and Astronautics
1801 Alexander Bell Drive, Suite 500, Reston, Virginia 20191-4344

ICING ANALYSIS AND TEST OF A BUSINESS JET ENGINE INLET DUCT

Kamel Al-Khalil*, Richard Hitzigrath†
Cox & Company, Inc., New York, NY 10014

Oliver Philippi‡
VisionAire Corporation, Chesterfield, MO 63005

Colin Bidwell‡
NASA Glenn Research Center, Cleveland, OH 44135

ABSTRACT

A program was developed to design an inlet duct anti-icing system of a light jet passenger aircraft. The inlet system consists of two offset "S-Shaped" intakes that provide air to a single jet engine after joining together at the engine face. Experimental and analytical methods were used in a combined approach to predict the impingement limits, ice mass interception, and power required for maintaining the internal inlet surfaces free of ice. A full-scale model of an inlet duct was constructed with integral heaters and placed in the Cox Icing Wind Tunnel. The test series included icing runs to investigate the impingement limits at various cloud droplet diameters conditions. The analytical methods used a full Navier-Stokes CFD solver and the NASA LEWICE3D ice accretion code.

1.0 SUMMARY

A program was developed to design a thermal ice protection system for a light business jet engine inlet duct. It is emphasized that this study considers the duct only. The inlet lip is a separate effort. The design process involved analytical predictions as well as icing tunnel tests that were conducted at the Cox LeClerc Icing Research Laboratory (LIRL). This report documents some of the experimental investigations and power predictions using 3-D computational tools. The analysis uses full Navier-Stokes Computational Fluid Dynamic (CFD) flowfield solutions. The computational model includes the fuselage, inlet ducts, and the vertical stabilizer but neglects the wings and horizontal stabilizers. Droplet impingement analysis is achieved using the NASA LEWICE3D ice accretion code. Analysis was performed for several droplet diameters and the results were integrated over the spectrum of droplet sizes to predict the total water catch at a particular Liquid Water Content (LWC) and droplet Mean Volume Diameter (MVD). The Langmuir "D" distribution was assumed valid during the design and analysis process.

*Engineering Scientist & Manager, Member AIAA
†Senior Mechanical Engineer, Member AIAA
‡Aerospace Engineer, Member AIAA

Copyright © 2000 by the American Institute of Aeronautics and Astronautics, Inc. All rights reserved.

2.0 EXPERIMENTAL STUDIES

2.1 Inlet Tunnel Installation

The single engine jet shown in Figure 1 is equipped with a bifurcated inlet duct. Two "S-Shaped" ducts join at the engine compressor inlet. A prototype model of the RHS (Right Hand Side) inlet was installed in Test Section-1 of the LIRL icing tunnel for testing. The primary goal was to determine the impingement zone(s) inside the duct.

The icing wind tunnel in the LIRL facility, shown in Figure 2, can simulate airspeeds in excess of 200 mph at temperatures as cold as –22 °F in it's upstream Test Section-1. This section measures 28 inches wide by 46 inches high by 6.5 ft long. The tunnel has a long straight diffuser between this main test section and the larger (48"x48")Test Section-2 downstream.

The tunnel installation is shown in Figures 3a and 3b. The duct was installed with the leading edge

near the tunnel floor in Test Section-1, and the duct trailing edge near the tunnel ceiling within the diffuser between the two test sections. The duct was inverted because of geometrical constraints within the tunnel and to maintain a flow parallel to the inlet mouth. Mounting was solid at both ends to prevent motion of the duct, which was verified during testing.

2.2 Aerodynamic Survey

Prior to the icing tests, an aerodynamic survey was performed to evaluate the effective airspeed in the tunnel and the airflow rate through the duct. Static pressure taps were installed in the throat region, near the upstream end of the duct. A pitot probe was also used to obtain the inlet dynamic pressure. The combination of pressure data and the throat area were used to compute the airspeed at the inlet and the airflow rate through the duct.

Because of the large blockage effects of the duct, the tunnel airspeed was limited to about 140 mph during icing tests. However, the aerodynamic survey showed that the flow through the inlet was equivalent to an airspeed of about 165 mph.

2.3 Impingement Studies

The water droplet cloud was generated using NASA MOD1 type nozzles. The droplet size distribution was calibrated using laser-measuring technology: Forward Scattering Spectrometer Probe (FSSP) and the Optical Array Probe (OAP) made by Particle Measuring Systems.

As a result of the complex S-Shaped and twisted duct geometry, droplet impingement was expected to be very sensitive to droplet Mean Volume Diameter (MVD). Therefore, the effect of various droplet sizes was investigated during the initial icing tests on an unheated duct. Table 1 shows the various conditions considered in the experimental impingement studies performed in the icing wind tunnel.

The atomizing nozzles used to create the cloud provide a droplet distribution that is fairly close to a Langmuir "D" distribution at MVD's near 22 microns and smaller. However, at larger diameters the cloud droplet distribution becomes progressively more skewed towards the larger size droplets that fall outside of the Langmuir distribution for a given droplet MVD.

Table 1: Impingement Survey Test Conditions

Run #	T_{amb} °F	Cloud notes	MVD µm	LWC g/m^3	Time min	V mph
1	0	(1)	15	0.6	5	141
2	0	(2)	60	1.4	5	141
3	22	(3)	60	2.2	8	141
4	22	(4)	28	1.1	6.5	141
5	20	(5)	23	1.0	14	141
6	0	(6)	21	1.0	24	141

Notes:
1. Cloud close to Langmuir-D distribution
2. Cloud skewed to include larger droplets than Langmuir-D distribution of same MVD
3. Same as Run 2
4. Cloud distribution simulates the right large droplet side of a 40 microns Langmuir-D distribution
5. Similar to the Run 4 cloud but slightly smaller droplets
6. Close to Langmuir-D with the larger droplets near 40 microns diameter

The following paragraphs provide a descriptive summary of the results:

Run 1:

The cloud of Run 1 provides a good look at ice collection resulting from small droplet sizes. No appreciable ice was observed. Mostly, white frost was seen in the duct that could be attributed to the common icing tunnel turbulence. Although negligible, it was noticeable from the light ice trace where ice had directly impinged on the surface. This impingement is a result of a very low volume of large droplets in the cloud particle distribution spectrum.

Run 2:

Following the light ice accumulation in Run 1, a cloud of very large droplets was considered to investigate the effect of the other extreme. In this case, the MVD was about 60 microns. An icing zone was observed on the bottom side of the duct through the first bend. It starts at about 2 ft from the lip HiLite (HL), and extends back to about 5.5 ft from the HL. A second ice collection zone was observed near the duct exit edge. This could be enhanced impingement caused by exit flow field effects.

Run 3:

This run was essentially a repeat of the second with a warm ambient temperature and a longer icing duration. The purpose was to investigate icing in glaze conditions. Essentially, the same impingement zone was observed; but the ice was more glaze-like, forming a more continuous and

thicker ice sheet with fewer ice "feathers" or "nodules". These feathers appeared to be breaking up at the aft end of the forward impingement zone.

Runs 4 and 5:

As a result of the skewed cloud droplet size distribution towards the larger droplets, an attempt was made to find an MVD which exhibited similar droplet sizes towards the larger side of a 40 micron MVD in a Langmuir "D" distribution. It is important in this case to simulate the correct impingement for droplets up to 40 microns MVD since that is the limit of the FAR-25C Continuous Maximum (CM) icing envelope.

The impingement zone observed was similar to Runs 2 and 3 but smaller. The forward edge of the first zone was about 2.5 ft instead of 2 ft from the HL. The trailing edge remained the same near the inflection point of the duct geometry. Typical ice buildup is shown in Figures 4 and 5, for front and back views, respectively.

Run 6:

After 2 minutes, this run was stopped to view the impingement zone after a short burst of spray. The test was continued for a total of 24 minutes after which the ice accretion became more significant, especially in the forward icing zone, which started at about 2 ft from HL. There were many "ice feathers" near the center of the forward zone. Other areas of the duct appeared to be covered with in a very thin (< 0.1 inch) ice layer.

The accretion observed is consistent with "tangential" (low Beta) impingement. The collection efficiency is very low but builds rapidly on the feathers. Evaluation of the forward icing zone area is subjective and appears to be close to 900 in^2.

The aft-most zone was observed to collect ice during testing but was not confirmed due to the open ended duct to the free stream, whereas actual installation has the compressor inlet at this location. Numerical analysis confirmed minor droplet impingement as will be shown later.

The primary limitation of this test was airspeed, which was at about 60% of a typical design condition. If one assumes the effect of airspeed on the collection efficiency is small, the total catch can be obtained by scaling the LWC.

2.3 Heat Transfer Coefficients

Following the droplet impingement tests, the duct was fitted with 18 electro-thermal heater zones in the forward and main ice accretion zones for further testing in dry and wet icing environments. Then, several icing tests with the heated duct were conducted to evaluate the surface heat transfer coefficients and the power required to anti-ice the duct at different conditions. Results were used to extrapolate for actual aircraft flight conditions.

To simplify the testing, the two side rows of symmetric zones were grouped, reducing the total number of independently controlled channels to 12. There were 24 temperature sensors: two in each of the center 6 zones, and one in each of the side symmetric zones. Control of each heater was based on the lower temperature reading in each zone or a specified duty cycle. The Cox Thermal Test Management System (TTMS) was used to control the 12 channels and record data. Control is accomplished by pulse width modulation. Wall temperature control is therefore maintained up to 100% duty. At 100% duty cycle, the power density applied to each heater zone was about 10 W/in^2.

The time constant of the wall in the highly convective environment was quite short. Consequently, the time to reach steady state temperatures was also short. Recorded data were averaged over the steady state condition period to obtain mean wall temperatures and heat fluxes.

The goal of the first series of tests was to measure convective heat transfer coefficients in dry air conditions (no spray). The general approach to measuring heat transfer coefficients is to hold the surface temperature (T_{surf}) steady and measure the corresponding heat flux (q, W/in^2) in each zone. The heat transfer coefficient (h) is then derived as follows:

$$h = q / (T_{surf} - T_r)$$

where the recovery temperature T_r is defined based on the local flow and in the duct. For this test, the free stream static, total and recovery temperatures are all within 5°F of each other. The wall surface is controlled at a relatively high temperature (~100°F above ambient) to minimize errors.

These data can be used to extrapolate the power required to aircraft airspeeds not attainable in the tunnel. In general, the scaling parameters include air speed, air pressure, air temperature, and liquid

water content and droplet diameter. The primary parameters, which must be extrapolated from the test, are air speed and ambient pressure. These parameters affect the heat transfer coefficient and the water catch efficiency.

Scaling of the convective heat transfer coefficient (h) is accomplished through the Reynolds number (Re):

$$h = \text{Constant} * Re^{0.8}$$

This relationship is based on the assumption of turbulent flow. The test speeds correspond to Re $>10^6$.

Figure 6 shows the experimental dry heat transfer coefficient data compared to that which might be expected from various analytical models. The bottom four curves represent a range of possible models for flat plates and straight ducts, depending on surface roughness and entry length effects. The experimental results appear to be in excess of any of these models. This could be caused by the concave duct surface, which is similar to a turning vane. According to the equation shown in Figure 6, a good fit of the data is obtained by setting the exponents (n1) to 0.8 and (n2) to 1/3, and by setting the constant (C) to 0.052. This equation is then the basis for extrapolation to actual flight conditions in the analysis and design process.

2.4 Water Droplet Collection Efficiency

Water catch is derived by testing a fairly high wall temperature and a representative droplet cloud. A sufficiently high wall temperature assures that all of the water impinging in a zone will be evaporated within that zone. The water catch is then derived from the energy balance in each zone:

$$q_{A/I} = q_{conv} + q_{evap} + q_{imp}$$

where,

$q_{A/I}$ = Anti-ice heat flux
q_{conv} = convective heat loss
q_{evap} = evaporative heat loss
q_{imp} = sensible and kinetic energy contribution of the impinging water

The impingement term includes the collection efficiency term, which can be resolved through an iterative process, given all other variables from the experiment. The water collection efficiency increases as the inlet airflow rate increases. However, droplet inertia studies indicate that speed makes only a minor change in catch efficiency for representative airspeeds in this case.

The average collection efficiency was computed for each of the heater zones using the above equation. Of particular interest, in addition to defining the impingement limits, is the maximum collection efficiency that occurs near the center of the forward icing zone. For an MVD of about 21 microns and inlet airspeed of 165 mph, the computed collection efficiency at that location was 0.053, or 5.3%. This value will be compared later to the 3D droplet trajectories obtained using LEWICE3D.

3.0 LEWICE3D IMPINGEMENT ANALYSIS

3.1 Analysis Points and Design Conditions

One of the benchmark design conditions is Condition 9, shown in Table 2.

Table 2: Condition 9

Parameter	Value
Altitude (ft)	12,000
Ambient Static Temperature (°F)	23
TAS (Kts)	214
W_{fan} (lb/sec)	45
Flight Mach number	0.33
Inlet Throat Mach number	0.4
LWC (g/m^3)	0.5
MVD (microns)	21.6

Condition 9 is important because it represents a low speed loiter situation in CM icing conditions. At higher speeds, the recovery temperature is above freezing. Condition 9 defines the near-worst case in terms of total water impingement in a below freezing temperature environment. For an evaporative system, this is an important design condition, and the preferred mode of operation is evaporative.

At the time the LEWICE3D analysis was performed, the CFD flow solution for condition 9 was not available yet. Instead, Condition B in Table 3 was used because it was available and also because it represented a balanced flow condition (no suction or spilling) which is representative of low cruise. To obtain a comparison with Condition 9, it was assumed that the normalized local catch distributions in the duct (i.e. *Beta* characteristics) are about the same between these two conditions (B and 9). In both cases, the free stream Mach number is close to

the throat Mach number. It is expected that the catch efficiency would be slightly higher at the higher Mach number because of the higher droplet inertia. Consequently, using the Case B analytical predictions of *Beta* for should yield conservative water catch prediction for Condition 9.

Table 3: Flow Conditions Considered for Analysis

Case	AOA (deg)	TAS (Kts)	Alt (Kft)	T_{amb} (°F)	Mach amb	M_{throat}
A	1.22	350	22	-22	0.576	0.300
B	2.31	280	22	-22	0.461	0.461
C	4.81	200	22	-22	0.329	0.4
D	7.45	140	12	-22	0.230	0.4
E	15	120	0	-22	0.197	0.46

3.2 Icing Cloud Droplet Distribution

Because of the tangential nature of droplet impingement in the “S-shaped" duct, the effect of droplet distribution is very significant. It is a customary and acceptable practice to use the Langmuir “D” droplet distribution in the analysis of aircraft ice accretion. Figure 7 illustrates that distribution for MVD of 20 microns, and the selected droplet sizes used in the LEWICE3D calculations, namely: 10, 20, 30, and 40-micron droplet sizes. These sizes were analyzed individually and the combined MVD effect was obtained using the corresponding weighting functions (%LWC) shown in Figure 7.

3.3 LEWICE3D Icing Impingement Results: Case B

A CFD solution is one of the input requirements to the NASA LEWICE3D ice accretion code for the prediction of catch efficiency distribution. The Monte Carlo approach was used in which a 1024x1024 rectangular matrix of droplets was released from far upstream and their trajectories computed. This process was repeated for each of droplet sizes considered in the distribution. The information resulting from trajectories that strike the surface is used to compute the local droplet collection efficiency. Figures 8 through 11 show the numerical results of catch efficiency on the lip for droplet sizes 10, 20, 30, and 40, respectively. As expected, the smaller droplets were not affected by the fuselage geometry or by the positive angle of attack. However, the larger droplets with higher inertia were forced away from the lower lip, which produced higher concentrations near the lower corners of the lip sides, just above the missed region. This is clearly defined for the 30 and 40 microns cases as depicted in Figures 10 and 11. Also, since Case B represents a condition with a positive angle of attack (2.3 degrees), the shadowing effect of the fuselage was enhanced and is apparent in the ice accretion on the inlet lip.

The catch efficiencies inside the inlet duct for droplet sizes of 10, 20, 30, and 40 microns, respectively for Case B are shown in Figures 12 through 15. The 10-micron case shows no significant impingement. As the droplet size increases, the catch efficiency increases as expected. This was as high as 15% for the 40-micron case at the first bend in the duct.

The combined results obtained using the weighting functions in the Langmuir “D” distribution are shown in Figures 16 through 18 for the inlet duct, the inlet lip, and the entire aircraft, respectively. These results represent the effective catch efficiency distribution on the aircraft for a water droplet MVD of 20 microns. Note that the size of the forward icing zone is about 1000 in^2. This is higher than the 900 in^2 estimated from the LIRL test. The forward zone started at a shorter distance from the lip than was the case for the LIRL test. One possible reason for this difference is the positive angle of attack of 2.3 degrees used in analysis as opposed to an angle of attack near negative one-degree in the LIRL tunnel (due to geometric restrictions). Another possible explanation is the effect of the fuselage on the trajectories of larger droplets. Lastly, the higher speed would have contributed to the increase in the impingement zone as well as the collection efficiency magnitude.

The aft-most section of the duct was seen to collect ice during the LIRL testing. The analysis showed similar impingement in those regions but the resulting catch efficiency was not significant except for a small region shown in Figure 16b. This could be a numerical effect where trajectories of impinging droplets are almost tangential to the surface and the flow is close to separating.

The catch efficiency *Beta* is a non-dimensional parameter defined as follows:

$$Beta = m'' / (LWC\ V)$$

where,

m” = impinging water flux (mass of water/unit time/unit area)

LWC = liquid water content in the cloud (mass of water/unit volume of air)

V = aircraft speed

The following equation can be derived from the above to get a rough estimate of the accreted ice thickness at a given condition (LWC, V, and ice exposure time):

Ice thickness (in) = $1.91e^{-5}$ x *Beta* x LWC(g/m^3) x V(mph) x time(sec)

As an example, consider the aircraft nose in Figure 18. The maximum value of Beta is about 0.35. If one assumes that the aircraft is flying at 200 KTAS (230 mph) in a rime ice condition at OAT = -4 °F and LWC = 0.2 g/m^3 for 30 minutes, the resulting maximum ice thickness collected on the nose is 0.55 inch. Based on the analysis of Condition 9, the total amount of water impinging on the duct surface is about 0.17 lbm/min spread over a large surface area. This assumes that the collection efficiency computed from Condition B is valid for Condition 9.

3.4 Power Estimate

The inlet duct was analyzed at Condition 9 (Table 2) except that 20 microns MVD was used instead of 21.6 microns to evaluate the power requirements to achieve total evaporative anti-icing performance. The power required to protect the 1000 in^2 impingement area evaporatively was computed to be 5 kW per duct using the catch efficiency predicted for Case B. The actual catch efficiency is lower due to the lower airspeed of Condition 9. Consequently, total required power should be slightly lower.

The LIRL test results were compared to predictions at the location of maximum catch efficiency in the duct. This was near the center of the impingement zone, about 3 ft downstream of the leading edge lip. The tunnel data showed that, for this particular location of the duct, Beta = 5.3% whereas the LEWICE3D computer model showed Beta = 6.5% for Case B as shown in Figure 18. This is 23% higher peak than seen in the LIRL test. If the catch efficiency distribution were to be scaled down by 23% within the impingement zone, the resulting estimated power would be 4.2 kW per duct.

Based on LIRL test data, the projected power requirement for Condition 9 is 3.5 kW per duct. The larger prediction is due to the larger predicted impingement zone (1000 in^2 versus 900 in^2) and the higher catch efficiency. Considering the number of variables and steps involved in the analytical predictions, and some of the experimental limitations, the comparison between the extrapolated tunnel data and the analytical results is acceptable.

The heat transfer coefficients obtained experimentally and extrapolated analytically were within 10% to 15% of the LEWICE3D predictions. The latter were computed using an integral boundary layer methodology, which requires the surface pressure distribution and free stream conditions.

Condition 9 is a warm and high LWC condition as per FAA Part 25-C CM envelope. The power requirement decreases as outside air temperature decreases due to the fact that LWC decreases as temperature decreases. However, the anti-icing power reaches a minimum at a certain temperature and increases thereafter. This is because the convective heat losses overwhelm the evaporative losses at very low LWC and ambient air temperature. Based on the conservative numerical results of *Beta* of Case B, the power required was calculated at several ambient temperatures and the corresponding LWC values. These total estimates for both ducts are shown in Figure A next page. It is seen that the minimum power required (9.5 kW) occurs at OAT of 5 °F and the maximum power required (12.4 kW) occurs at OAT of –22 °F.

If a “clean” duct were required for the entire Continuous Maximum conditions described by FAR-25C, then the design point is at –22 °F. Figure A indicates that at this condition a total of 12.4 kW is required to anti-ice both inlet ducts electro-thermally. In practice, a slightly higher power is required to cover all the possible conditions in the flight envelope for the entire range of temperatures between –22 °F to near the freezing point.

Assuming power is limited to 10 kW for anti-icing both ducts, Figure A indicates that this power should be enough to provide protection down to about -7 °F OAT where the corresponding LWC is near 0.2 g/m^3 (FAR 25-C). The maximum collection efficiency in the duct is about 6.5%. Using these values of Beta and LWC with an airspeed of 214 Kts (Condition 9), the resulting maximum accumulated ice thickness would have been 0.17 inch in 45 minutes of ice exposure at temperatures below –7 °F OAT. The actual ice thickness would be less when the heater is activated since some of the impinging water will sublimate as a result of its higher temperature.

Also, it is expected that the actual collection efficiency would be lower.

4.0 Concluding Remarks

Based on the analytical predictions for Condition 9, between 8.4 kW and 10 kW power is required for an evaporative electro-thermal anti-icing system of the two engine inlet ducts. The increase in power prediction is attributed to the larger LEWICE3D computed impingement zone and higher catch efficiency compared to the results extrapolated from the LIRL testing. This is due to the higher speeds, fuselage effect on the flowfield, and the positive angle of attack, in addition to uncertainties associated with both of the experimental and computational predictions.

The use of icing tunnel data combined with LEWICE3D is seen to provide a viable procedure for design and analysis.

Acknowledgments

Permission to use the preceding results and the support of this program by the VisionAire Corporation is acknowledged and appreciated. Special recognition is made to Mr. Kenneth Yeoman (deceased) for his dedication and technical guidance during this project.

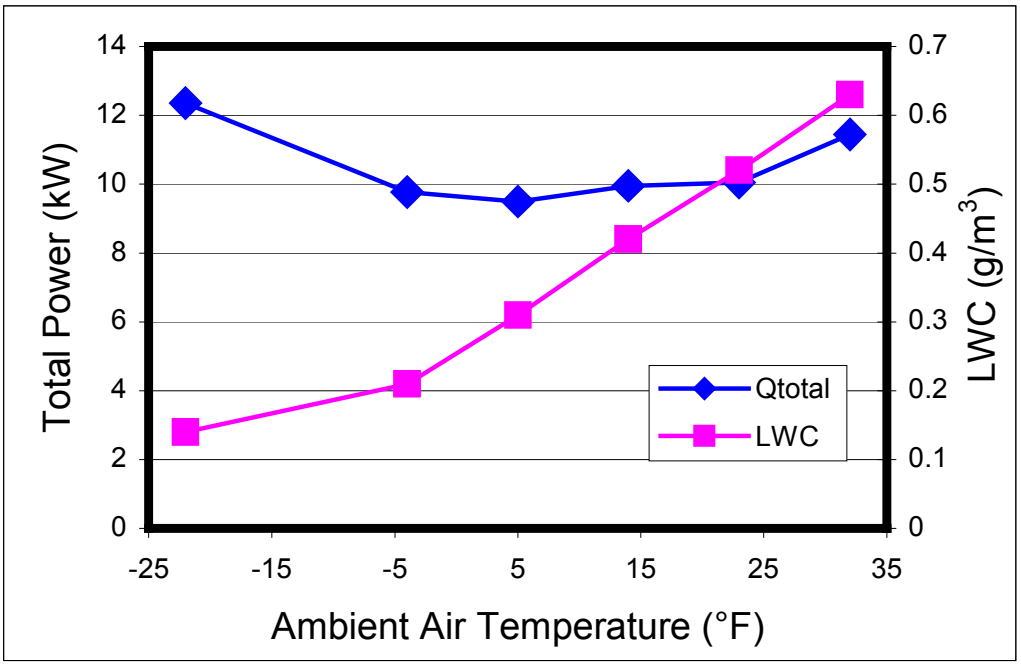

Figure A: Total Power Required to Anti-Ice both Inlet Ducts as a Function of Ambient Temperature

Figure 1: Single Engine Aircraft in Flight (Courtesy of VisionAire Corp.)

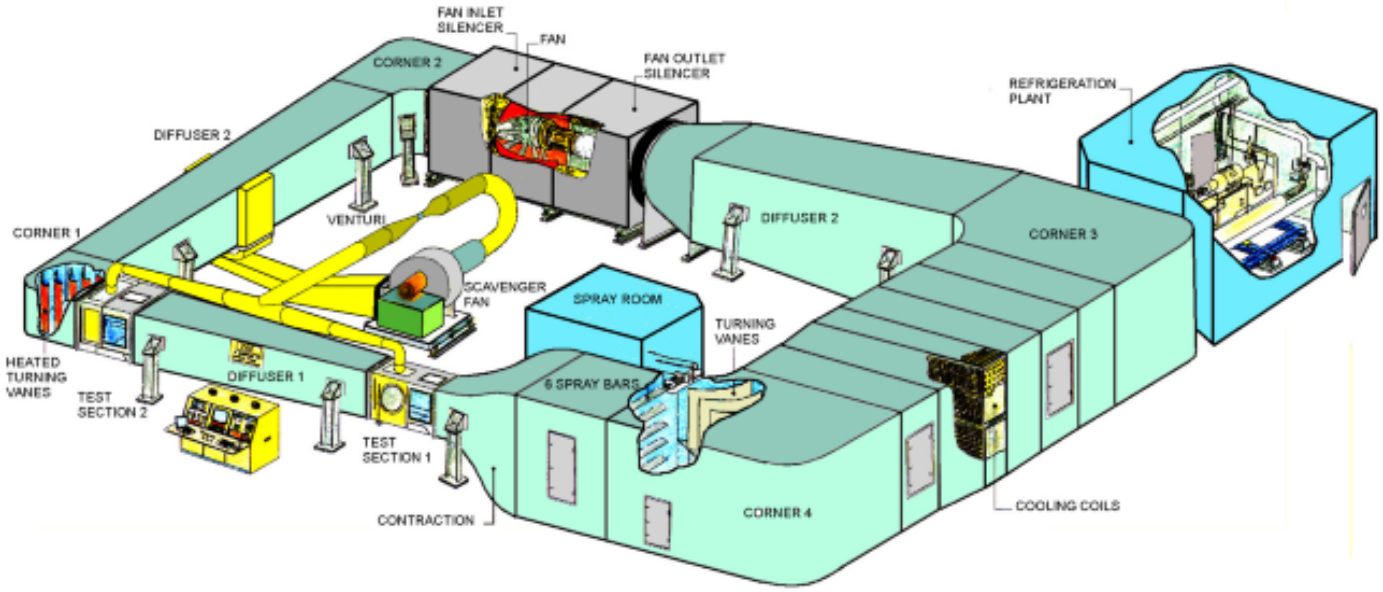

Figure 2: Layout of the Cox Icing Wind Tunnel at the LeClerc Icing Research Laboratory (LIRL)

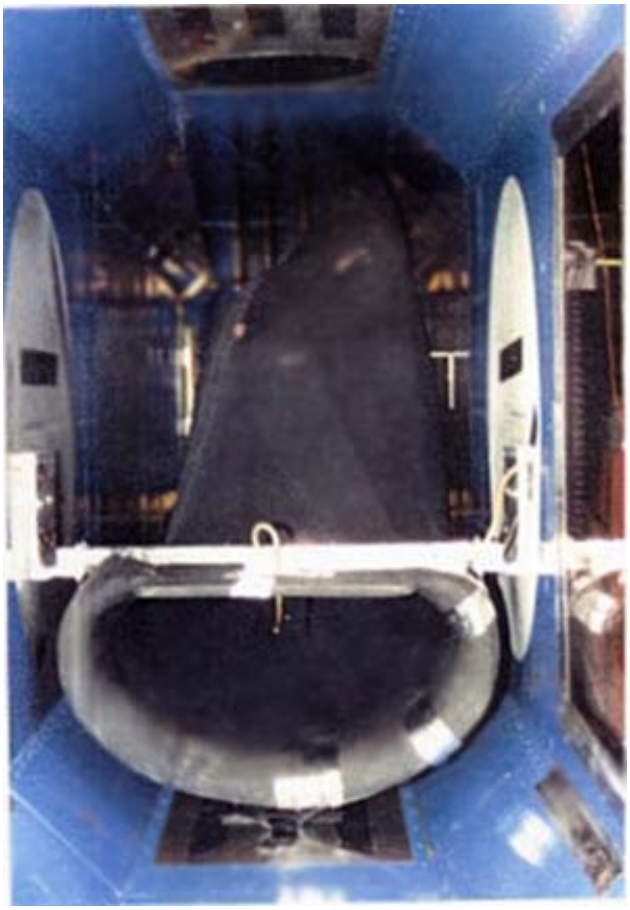

Figure 3a: Leading edge view of the inlet duct tunnel installation

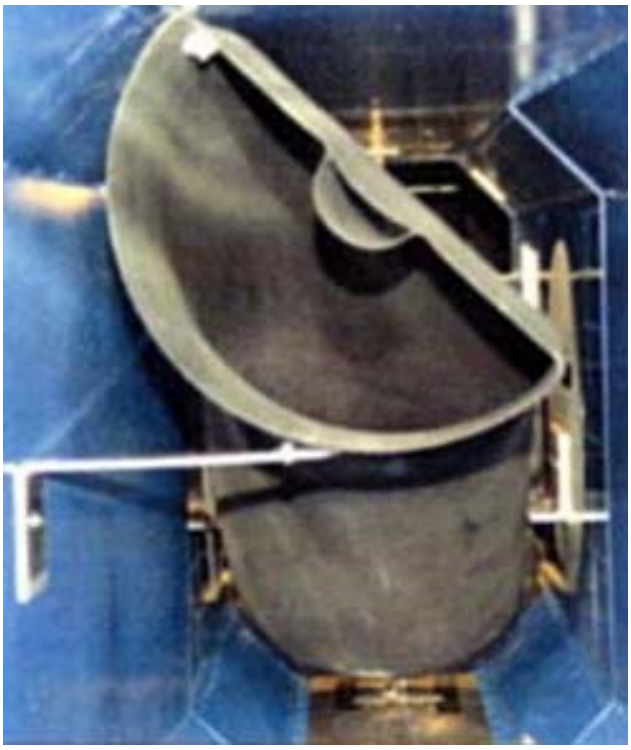

Figure 3b: Trailing edge view of the inlet duct tunnel installation

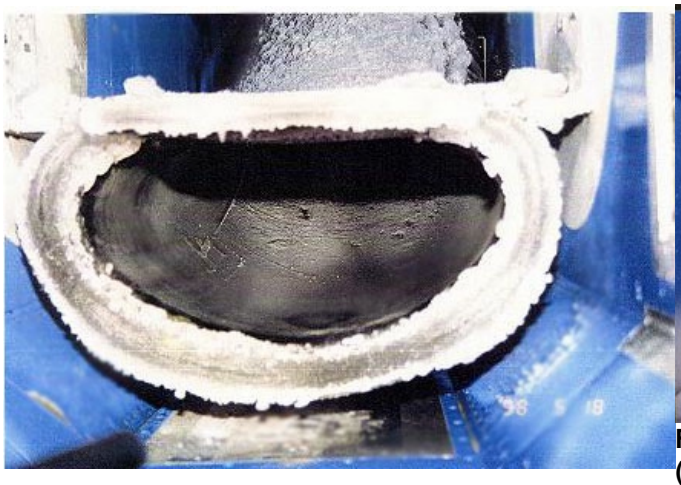

Figure 4: Typical ice accretion on the duct (leading edge view)

Figure 5: Typical ice accretion in the duct (trailing edge view)

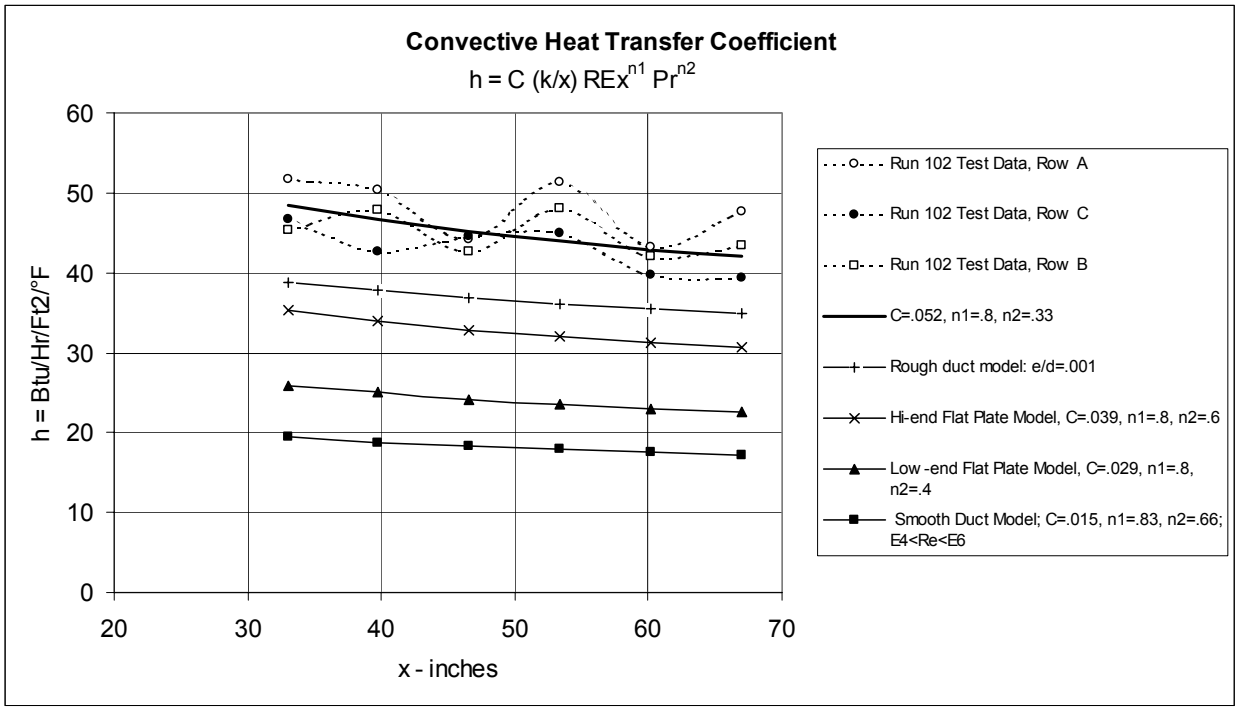

Figure 6: Experimental dry heat transfer coefficient data

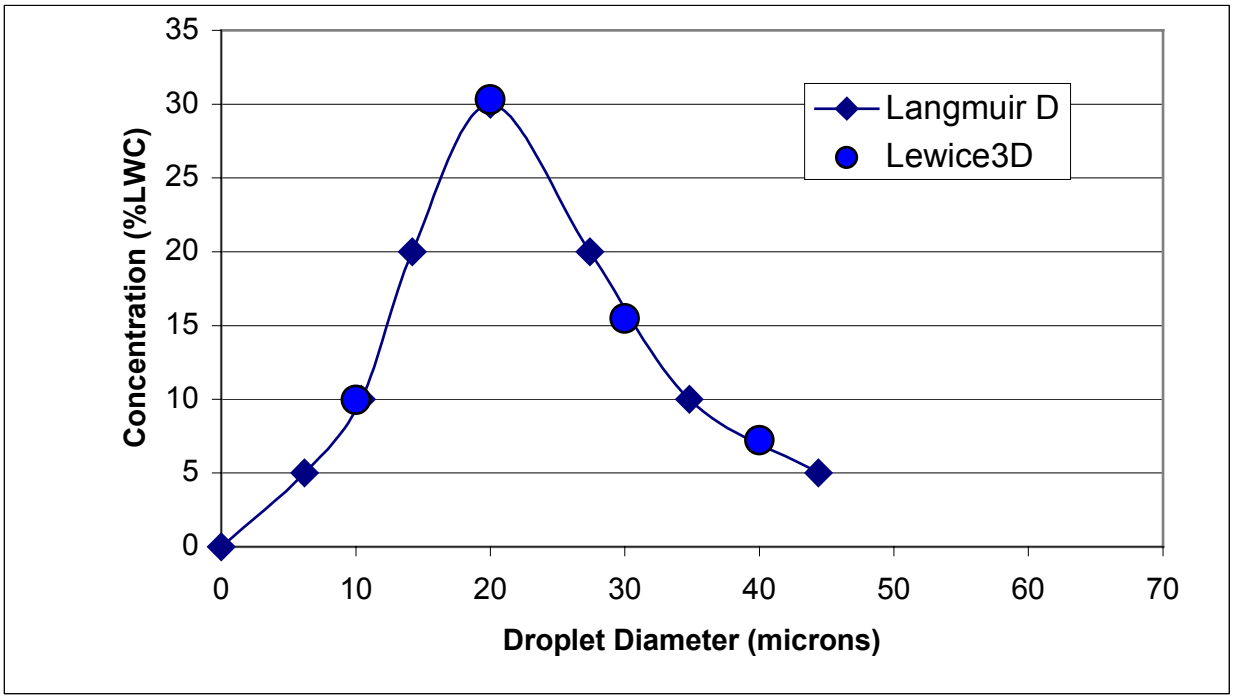

Figure 7: Droplet Distribution used in the LEWICE3D Droplet Analysis

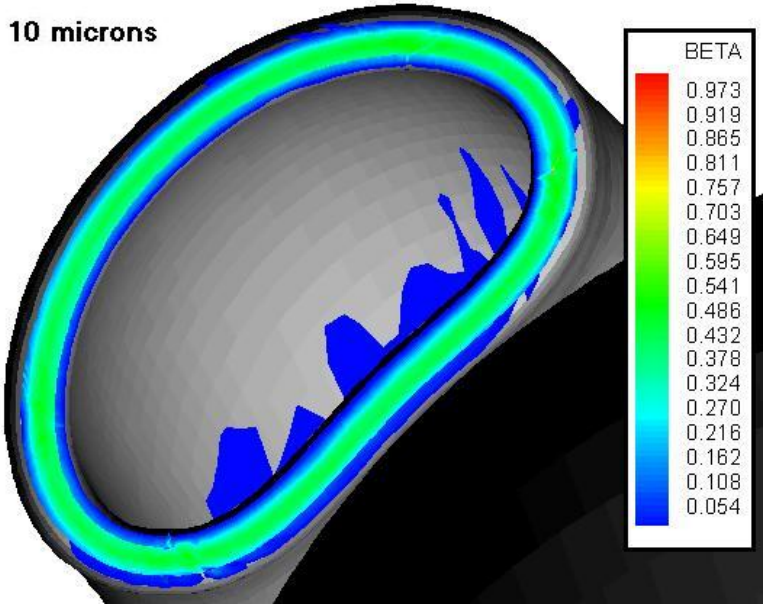

Figure 8: Lip Catch Efficiency for 10 microns (Case B)

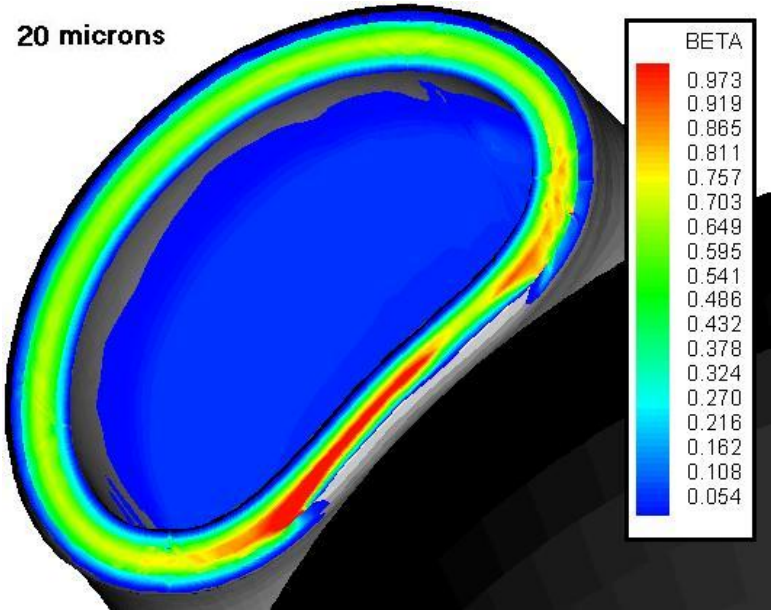

Figure 9: Lip Catch Efficiency for 20 microns (Case B)

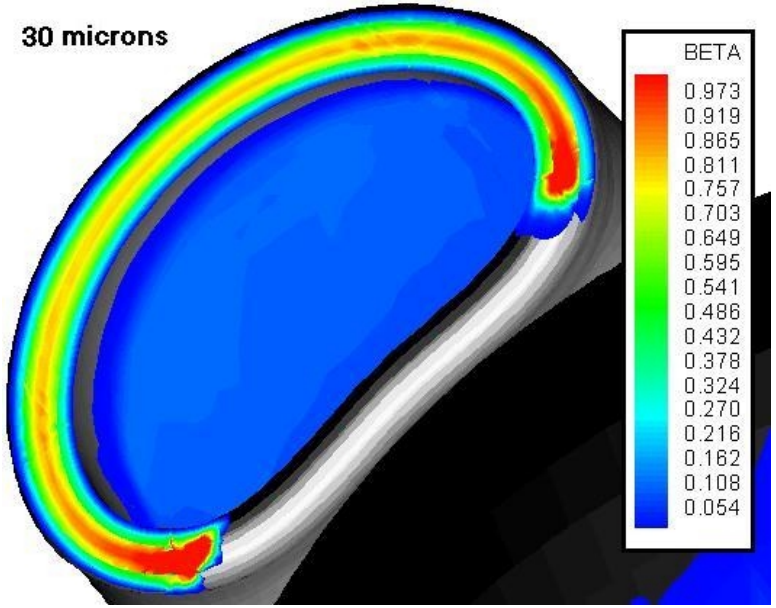

Figure 10: Lip Catch Efficiency for 30 microns (Case B)

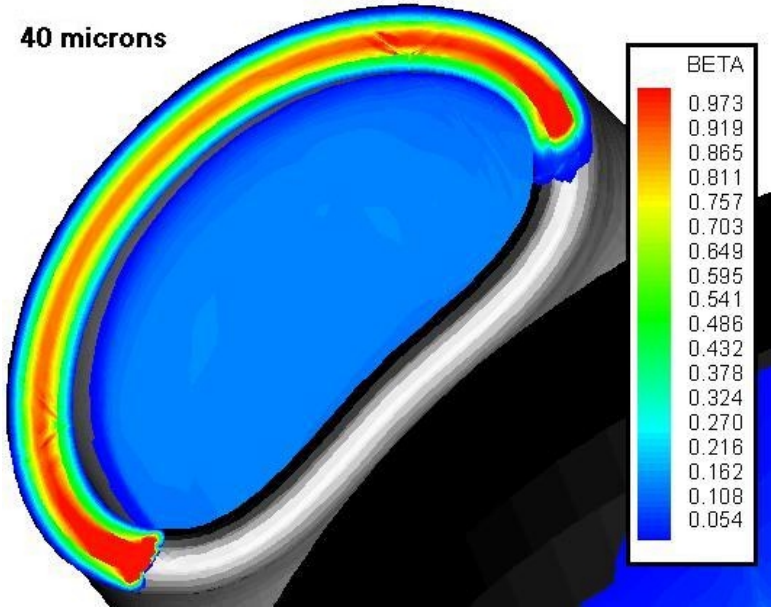

Figure 11: Lip Catch Efficiency for 40 microns (Case B)

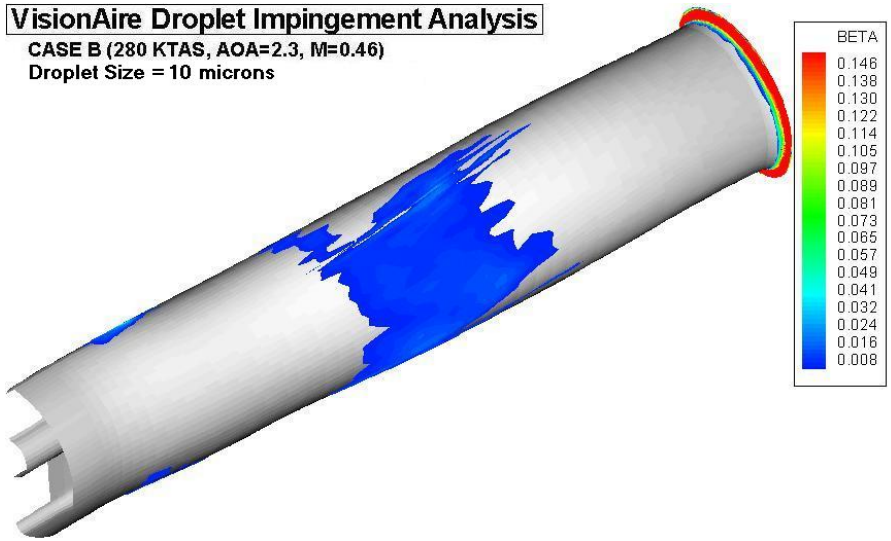

Figure 12: Duct Catch Efficiency for 10 microns (Case B)

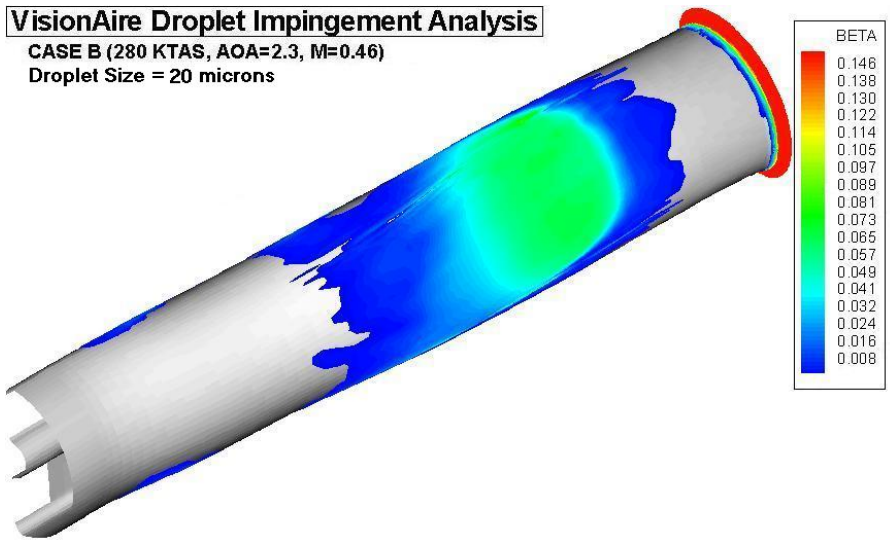

Figure 13: Duct Catch Efficiency for 20 microns (Case B)

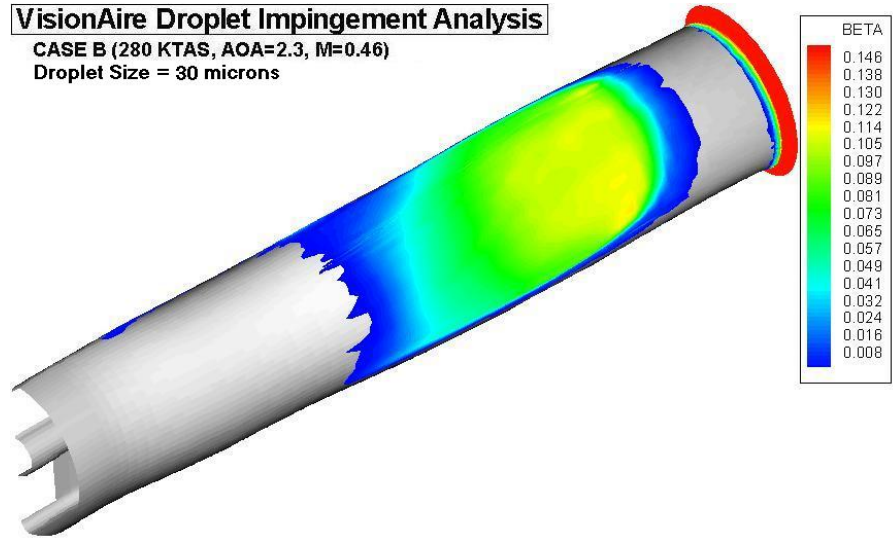

Figure 14: Duct Catch Efficiency for 30 microns (Case B)

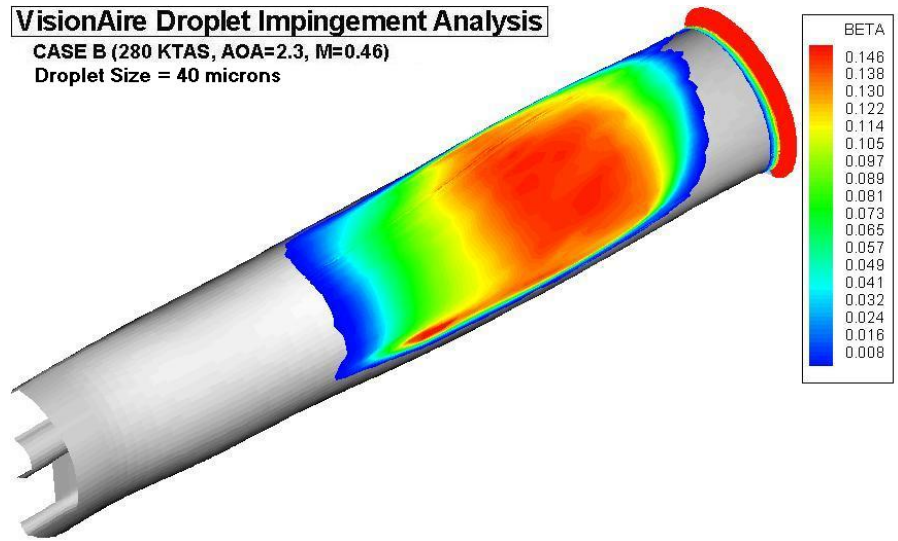

Figure 15: Duct Catch Efficiency for 40 microns (Case B)

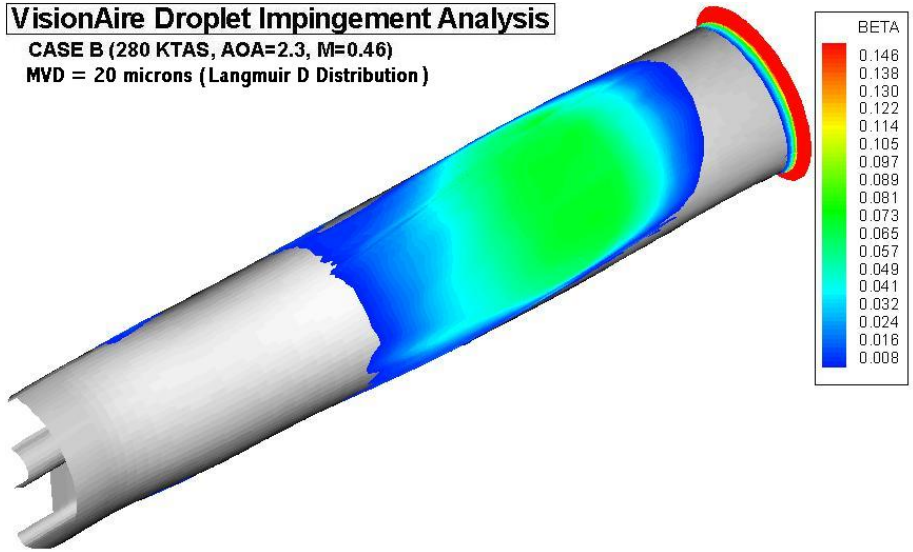

Figure 16a: Duct Catch Efficiency for MVD=20 (Case B)

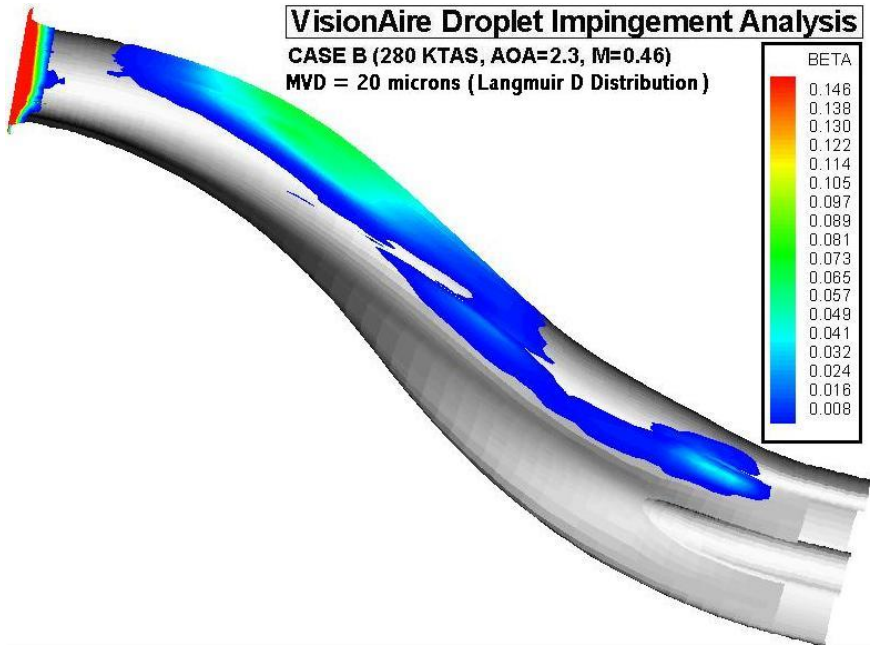

Figure 16b: Duct Catch Efficiency for MVD=20 (Case B)

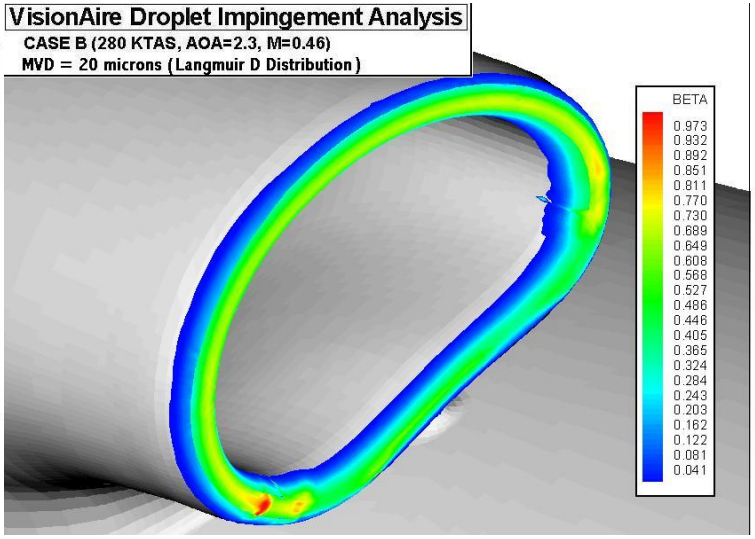

Figure 17: Lip Catch Efficiency for MVD=20 (Case B)

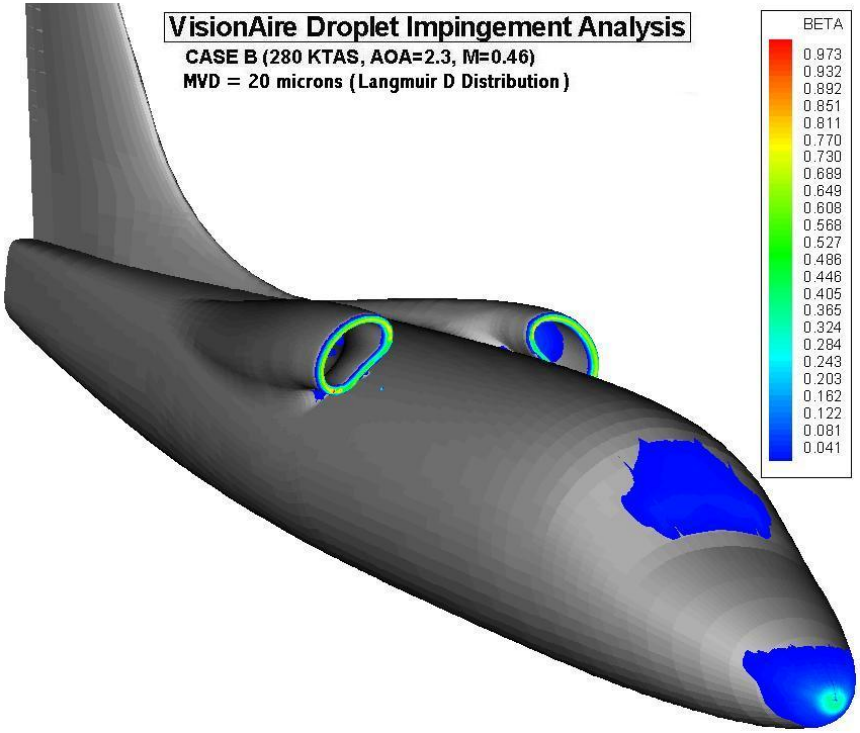

Figure 18: Aircraft Catch Efficiency for MVD=20 (Case B)